

# Simultaneous Measurement of 10,000 Protein-Ligand Affinity Constants Using Microarray-based Kinetic Constant Assays

J. P. Landry, Y. Y. Fei, and X. D. Zhu\*

*Department of Physics, University of California at Davis, Davis, California, 95616, USA*

\* Corresponding Author, [xdzhu@physics.ucdavis.edu](mailto:xdzhu@physics.ucdavis.edu)

## SUPPLEMENTAL MATERIALS

### OI-RD Scanning Microscope Control

Microscope control, data acquisition, image processing/analysis, binding curve processing/analysis (nonlinear curve fitting), and report generation are performed with a custom application suite developed in LabVIEW 7 (National Instruments, Austin, TX) by ourselves.

### Microarray Printing Conditions

The microarrays were printed at ambient temperature ( $\sim 25^\circ\text{C}$ ) and elevated relative humidity ( $\sim 65\%$ ). The target materials were dissolved in  $1\times$  PBS (pH 7.5) to desired concentrations for printing. Primary amines on the target protein surface bind covalently to the epoxide groups on the glass surface. The printing robot was equipped with eight silicon  $100\ \mu\text{m}$  quill pins (Parallel Synthesis, Santa Clara, CA). The centers of the printed spots were separated by  $250\ \mu\text{m}$  and the diameters of the spots varied from  $80\ \mu\text{m}$  to  $160\ \mu\text{m}$  depending on the concentration and the wetting properties of the printed solution. The printed microarrays were stored in a slide box for a minimum of 12 hours before further processing.

### $K_a$ Maps of Eight Protein Probes Against the 10,880-spot Target Microarrays Shown in Fig. 6

We measured binding curves of eight protein probes against the 10,880-spot target microarray (**Figure 6**) by sequentially exposing the microarray to solutions of these probes at one

concentration. In order of reactions, the 8 protein probes were anti-phenobarbital IgG, concanavalin A (lectin), anti-theophylline IgG, anti-biotin IgG, anti-tetrahydrocannabinol IgG, anti-morphine IgG, anti-dinitrophenol IgG, and anti-methamphetamine IgG. We repeated the reaction sequence with different probe concentrations on fresh microarrays to obtain 10,880 sets of binding curves for each printed target. **Figure S-1** through **Figure S-8** display  $K_a$  maps (equilibrium association constants) of these eight proteins against the 10,880 targets, representative sets of binding curves for each probe, and the histogram of  $K_a$  for each probe against the same specific targets but printed at different locations. We show the means and the standard deviations of the association rates, dissociation rates, and equilibrium association constants of eight specific probe-target pairs in Table 1.

It is clear that there is noticeable cross reactivity of mouse anti-theophylline IgG to dinitrophenol-BSA targets, albeit with an order of magnitude smaller  $K_a$ . For concanavalin A, in addition to specific binding to glucose-BSA targets, the protein also binds to a number of immobilized IgG targets.

FIGURE S-1

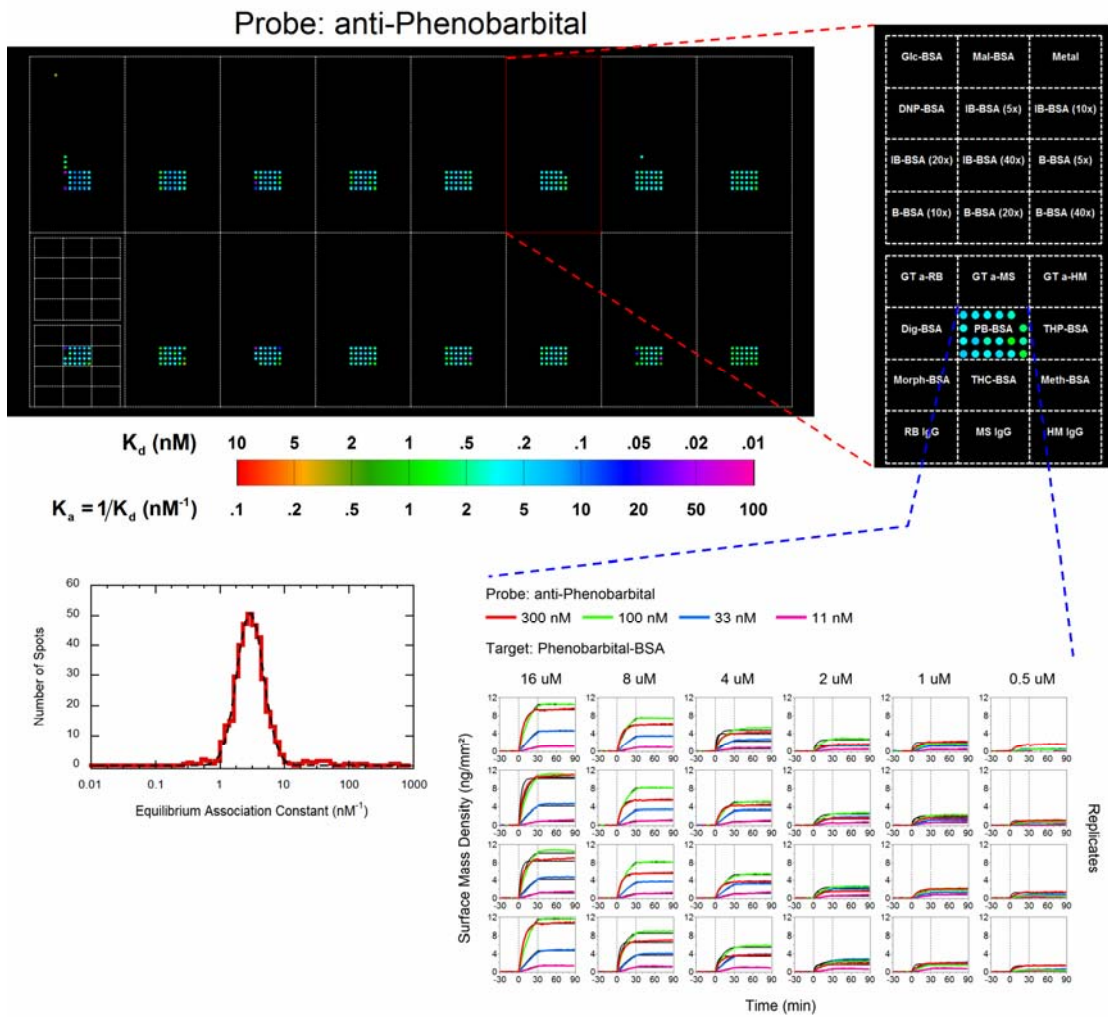


FIGURE S-2

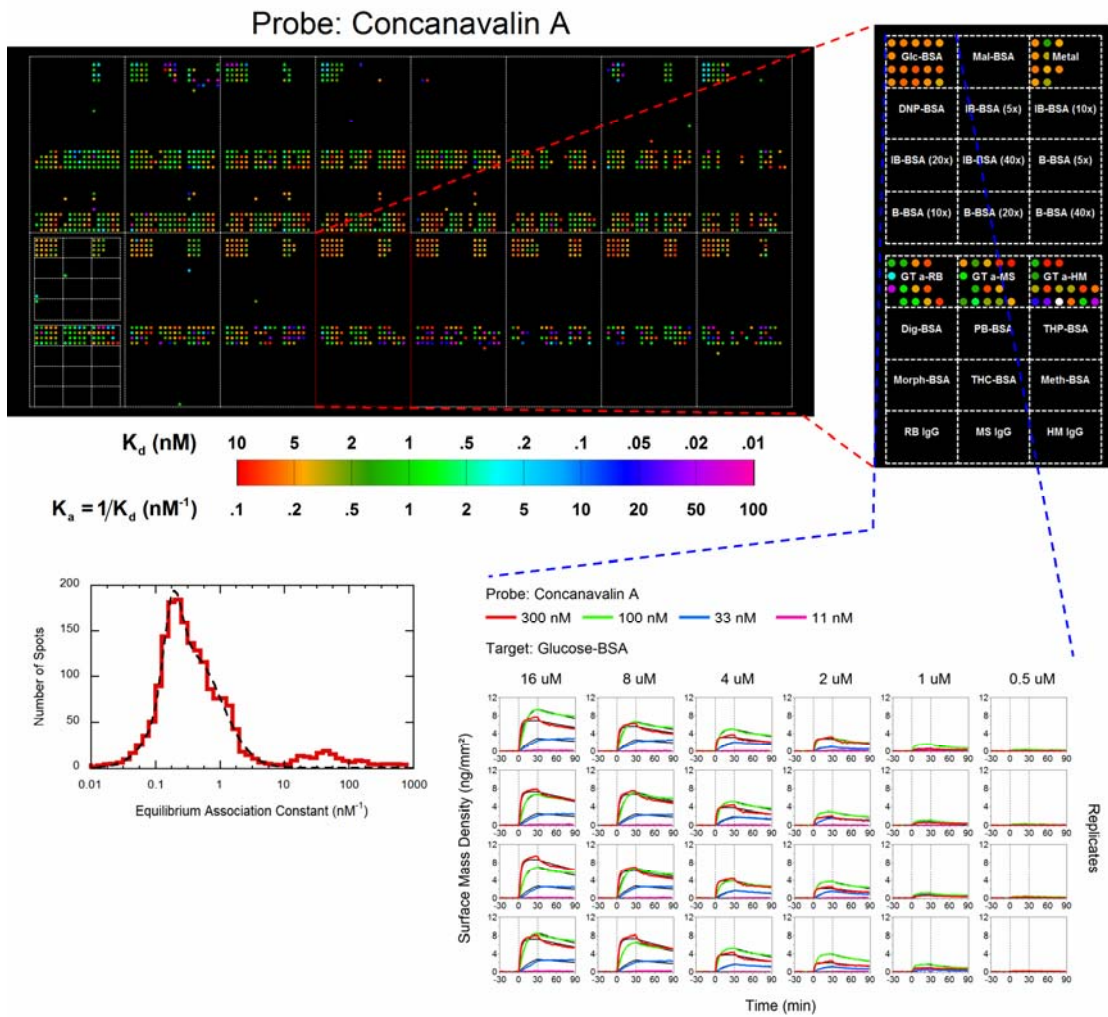


FIGURE S-3

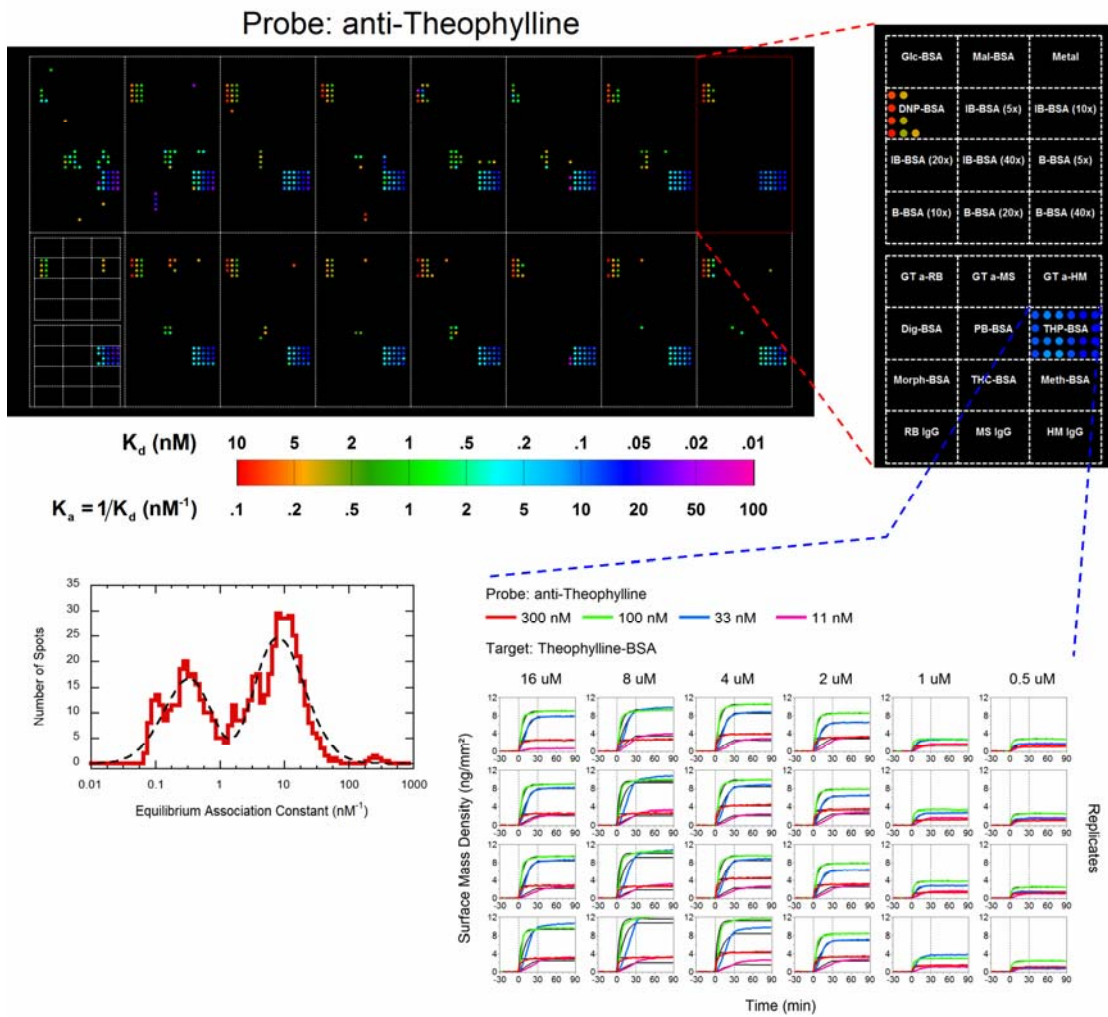


FIGURE S-4

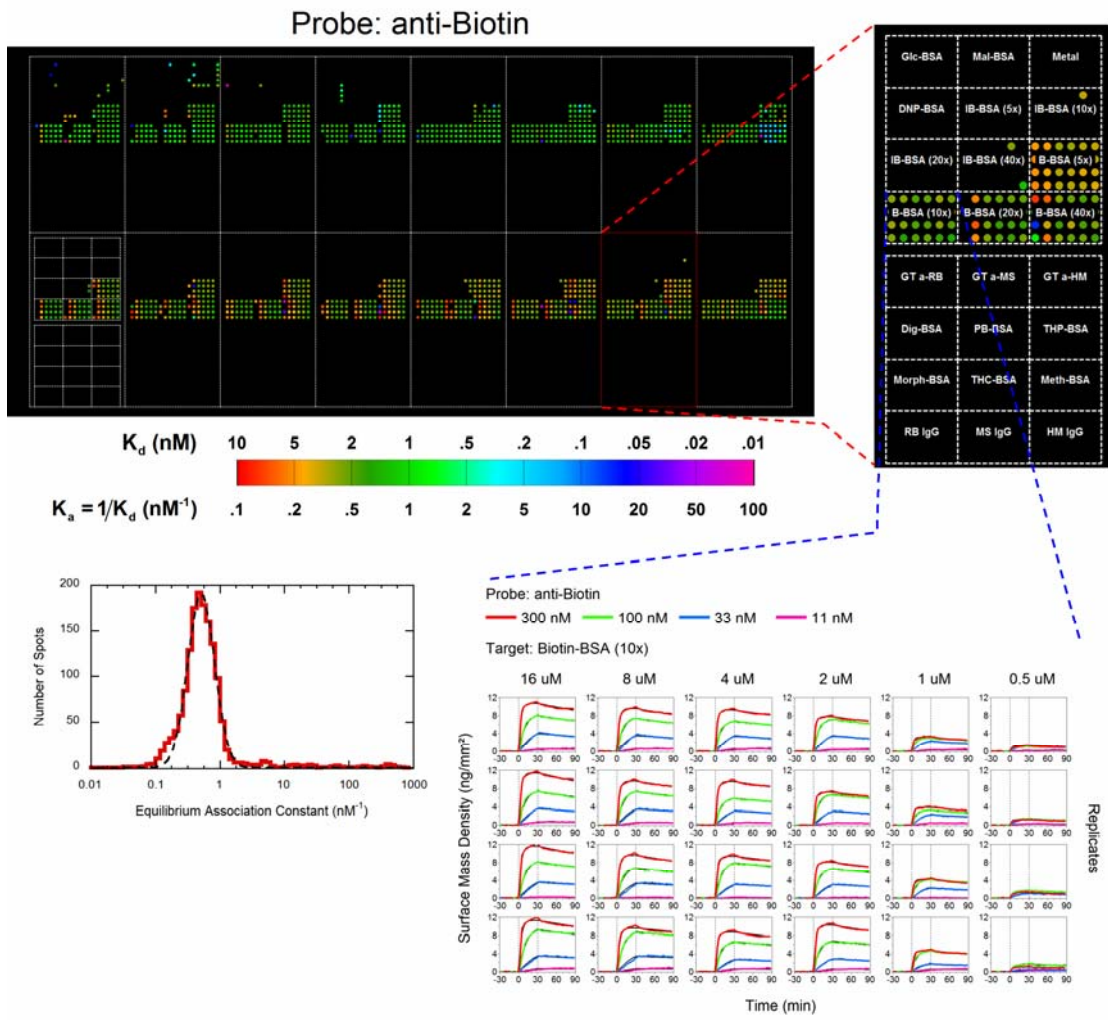


FIGURE S-5

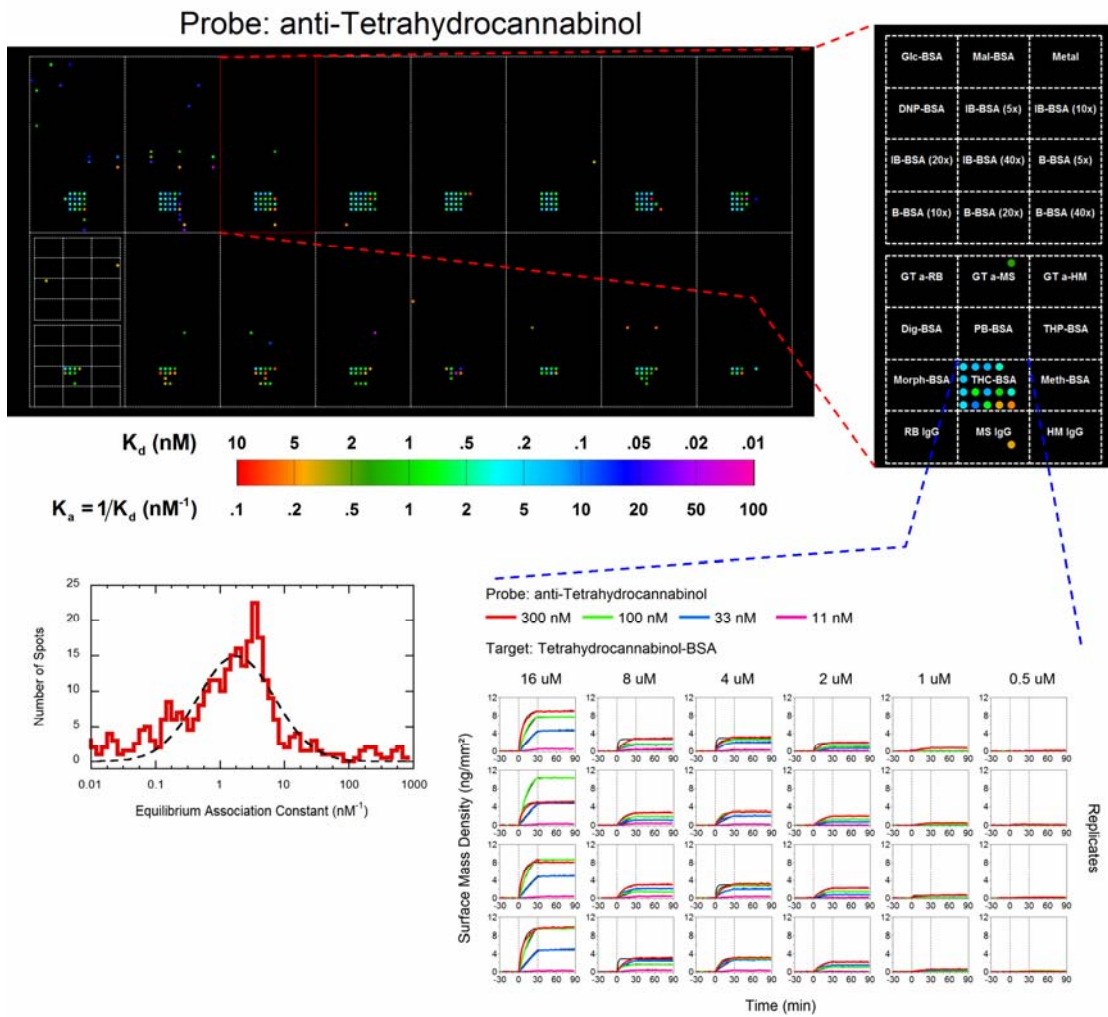


FIGURE S-6

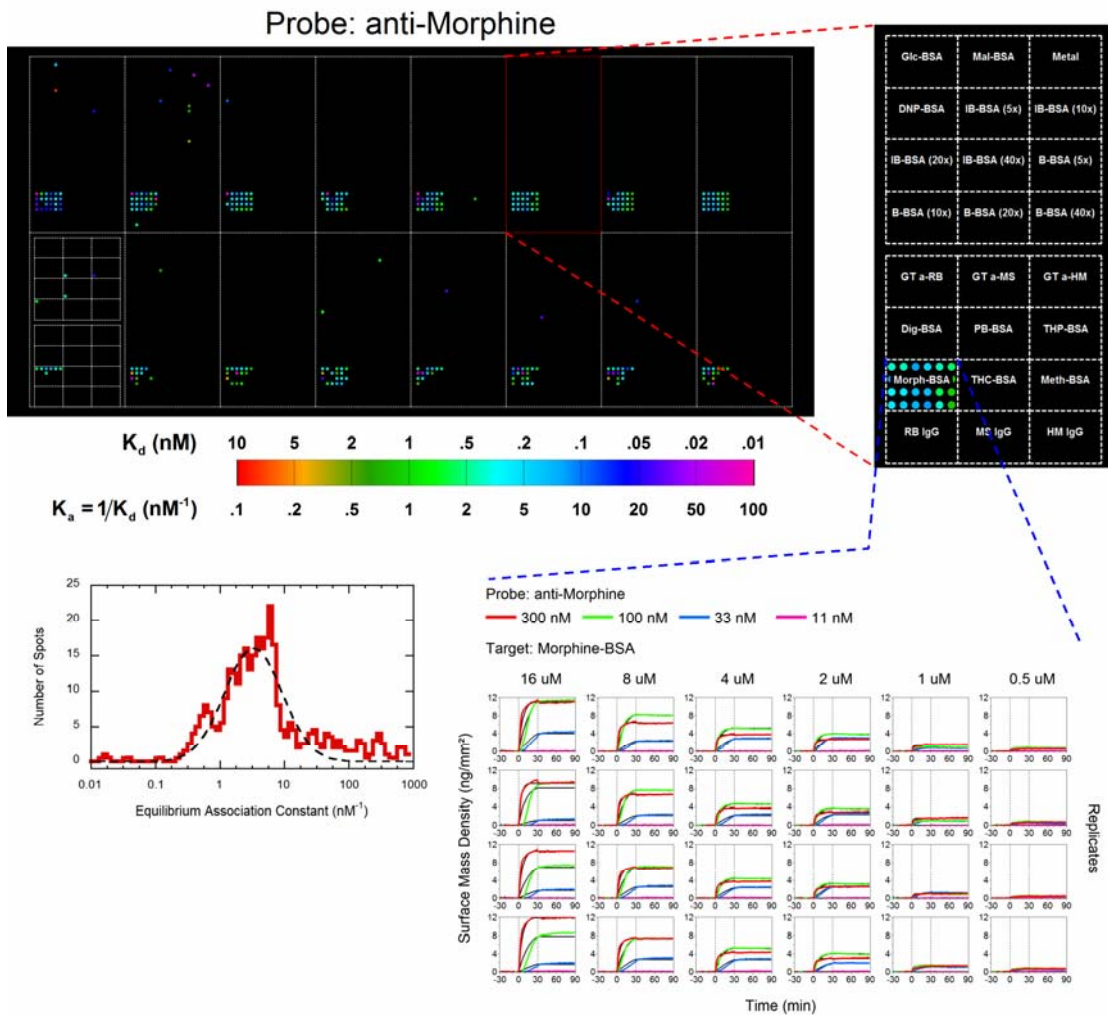


FIGURE S-7

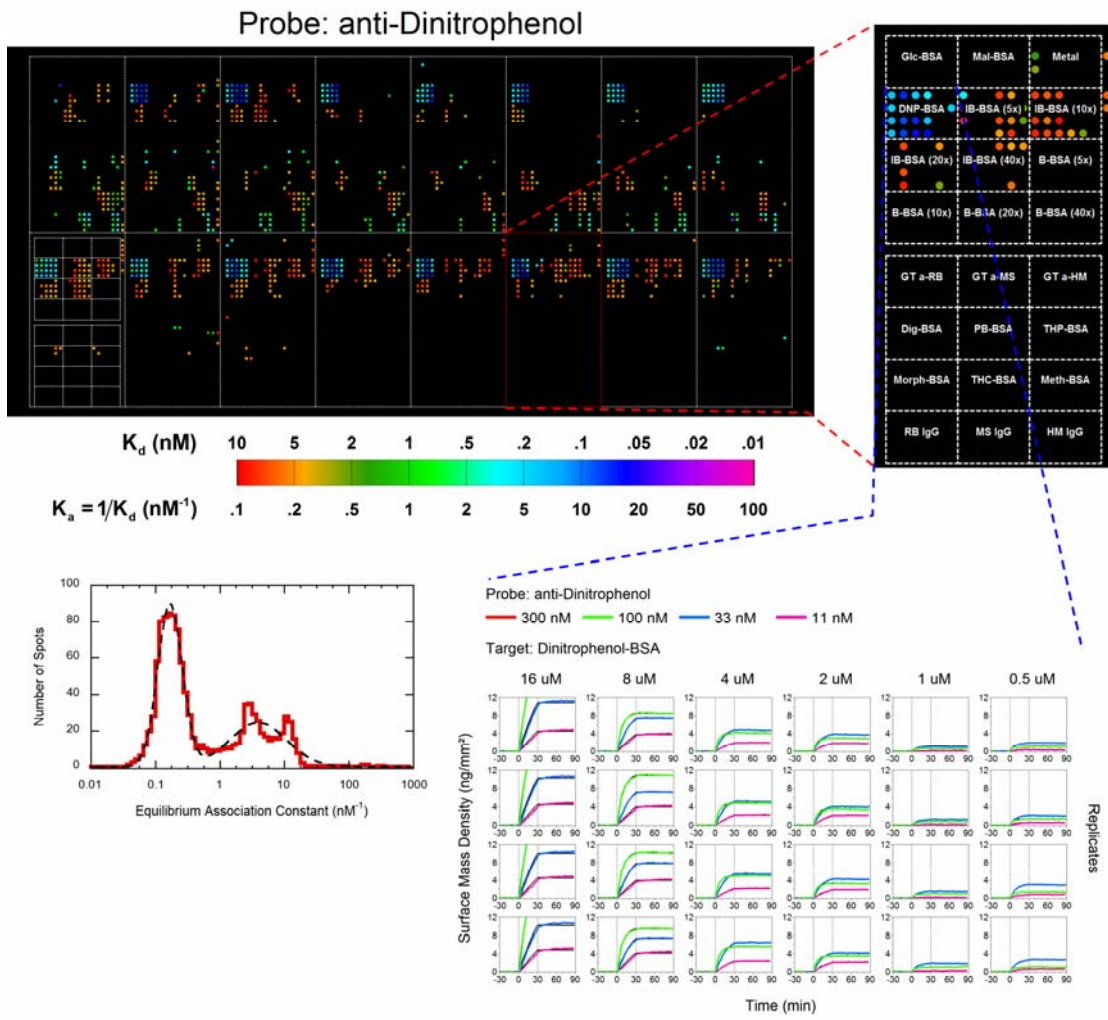
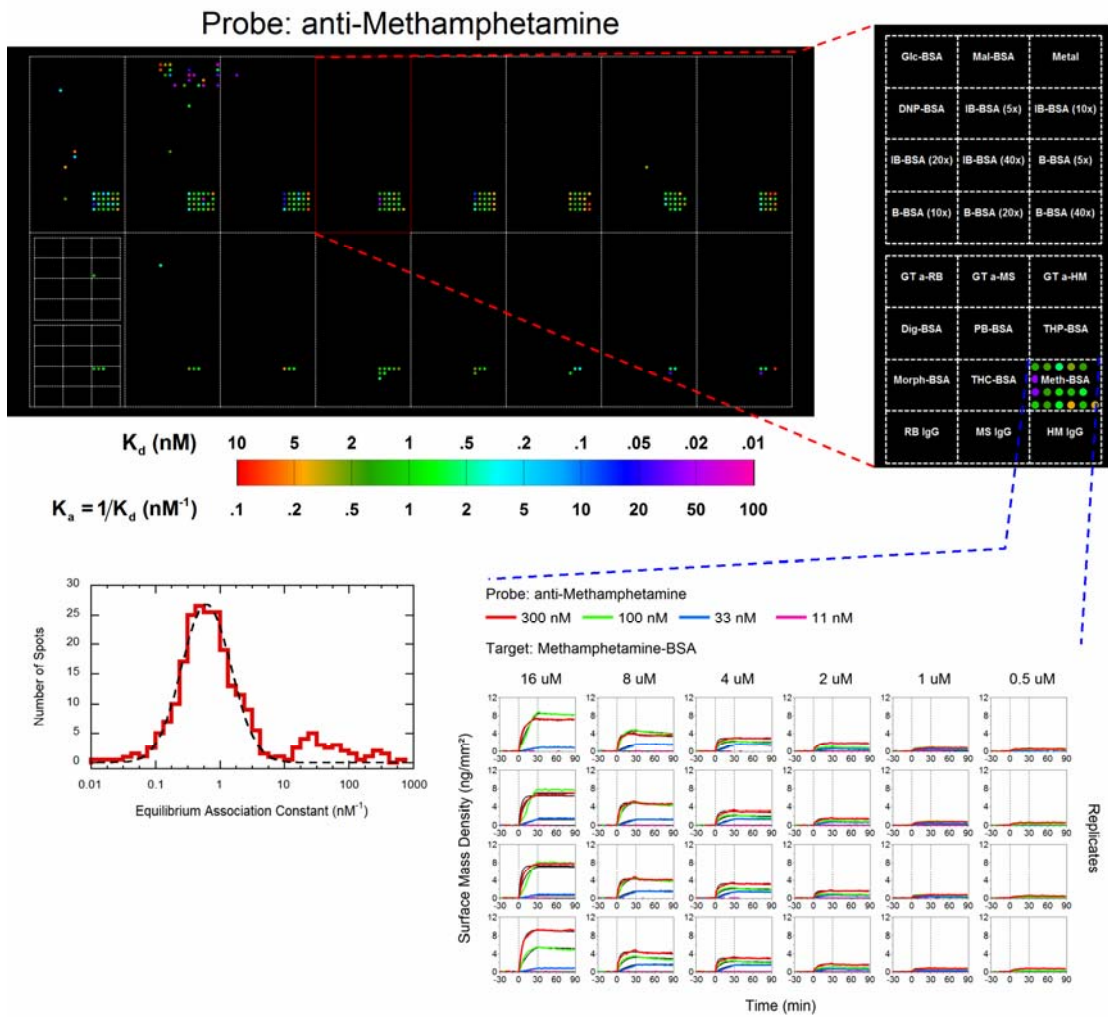


FIGURE S-8



**TABLE S-1:** Association rates, dissociation rates, and equilibrium association constants of eight protein probes with respective ligands (**Figure 6**). The values are 68% confidence intervals obtained from the mean and standard deviation of a Gaussian distribution fit to a histogram of values from *all* appropriate microarray spots (several hundred spots for each reaction). Values for each spot were obtained from nonlinear curve fitting to the Langmuir binding reaction model. We estimate from the data a 68% confidence *upper bound* for the dissociation rate (the association and dissociation rates must be nonnegative) where appropriate. They are comparable in value to the available affinity constants for some of monoclonal mouse anti-drug IgG molecules that Fitzgerald Industries International, Inc. provides commercially (<http://www.fitzgerald-fii.com/Products?pId=9&sId=21>).

Probe	Target	$k_{\text{on}} (\text{M}\cdot\text{s})^{-1}$	$k_{\text{off}} (\text{s}^{-1})$	$K_{\text{a}} (\text{nM}^{-1})$
anti-phenobarbital IgG	phenobarbital-BSA	$(1.3 \pm 0.1) \times 10^4$	$< 4.8 \times 10^{-6}$	$> 2.7$
concanavalin A	glucose-BSA	$(2.3 \pm 0.3) \times 10^4$	$(8.7 \pm 0.9) \times 10^{-5}$	$0.26 \pm 0.01$
	whole IgG	$(1.00 \pm 0.07) \times 10^4$	$(2.2 \pm 0.4) \times 10^{-5}$	$0.45 \pm 0.07$
anti-theophylline IgG	theophylline-BSA	$(3.4 \pm 0.3) \times 10^4$	$< 2.8 \times 10^{-6}$	$> 11$
	dinitrophenol-BSA	$(3.4 \pm 0.3) \times 10^4$	$(9 \pm 3) \times 10^{-5}$	$0.36 \pm 0.01$
anti-biotin IgG	biotin-BSA	$(2.2 \pm 0.2) \times 10^4$	$(4.5 \pm 0.5) \times 10^{-5}$	$0.53 \pm 0.06$
anti-tetrahydrocannabinol IgG	tetrahydrocannabinol-BSA	$(1.1 \pm 0.2) \times 10^4$	$< 9.1 \times 10^{-6}$	$> 1.2$
anti-morphine	morphine-BSA	$(2.1 \pm 0.2) \times 10^4$	$< 6.9 \times 10^{-6}$	$> 3.0$
anti-dinitrophenol	dinitrophenol-BSA	$(1.8 \pm 0.1) \times 10^4$	$< 7.2 \times 10^{-6}$	$> 2.5$
anti-methamphetamine	methamphetamine-BSA	$(1.6 \pm 0.2) \times 10^4$	$(2.2 \pm 0.4) \times 10^{-5}$	$0.72 \pm 0.1$

### Measurement of Reflectivity Phase Difference $\Delta\delta$

In this section, we provide details on how the OI-RD microscope measures the changes in the reflectivity phase  $\delta$ , where  $r_p/r_s = \tan\psi \cdot \exp(i\delta)$  and  $r_p$  and  $r_s$  are the complex  $p$ -polarized and  $s$ -polarized reflectivities, respectively. This microscope varies in several details from previously reported OI-RD microscopes<sup>1-4</sup>. In particular, this microscope is designed to measure changes in  $\delta$  exclusively (previous microscopes can also measure changes in  $\psi$ ). Since the OI-RD response with optically transparent substrates and protein layers is predominantly through  $\delta$ , the current microscope configuration sacrifices very little information in exchange for a simpler and more robust signal normalization scheme compared to previous OI-RD microscopes. However, it should be pointed out that the high-speed scanning mechanisms are independent of these details and therefore high-throughput kinetic measurements analogous to those described in the main text can be performed with the previous OI-RD configurations as well.

The arrangement of the optics in the OI-RD microscope is illustrated in Figure 1 and (for convenience) **Figure S-9** (top). A He-Ne laser beam of wavelength  $\lambda = 633$  nm and linearly polarized at angle  $P$  (from  $p$ -polarization) passes through a photoelastic modulator (PEM). The photoelastic modulator acts as a waveplate with a sinusoidally varying retardation of frequency  $\Omega = 50$  kHz and amplitude  $\pi/2$  (quarter wave). The axes of the PEM are aligned with the glass slide  $p$ - and  $s$ -polarization components. The beam passes through a phase shifter (e.g. a wave plate tilted about a principal axis) that adds an adjustable but static phase  $\Phi_{ps}$  between the  $p$ - and  $s$ -polarized components. The scan lens focuses the beam into a  $\sim 30$   $\mu\text{m}$  diameter spot on the microarray-bearing glass surface at incidence angle  $\theta = 36.6^\circ$  inside the glass slide. The microarray-bearing surface is immersed in an aqueous solution within the flow channel. The reflected beam from the illuminated spot passes through an analyzer with its transmission axis set at angle  $A$  (from  $p$ -polarization) and is imaged with an objective lens onto a long-profile photodiode. A slit in front of the photodiode passes the image from the back surface reflection and blocks the images from the front surface reflection and from multiple bounces within the glass slide. The first and second harmonic components of the resulting photocurrent are measured with lock-in amplifiers. Their signed amplitudes are

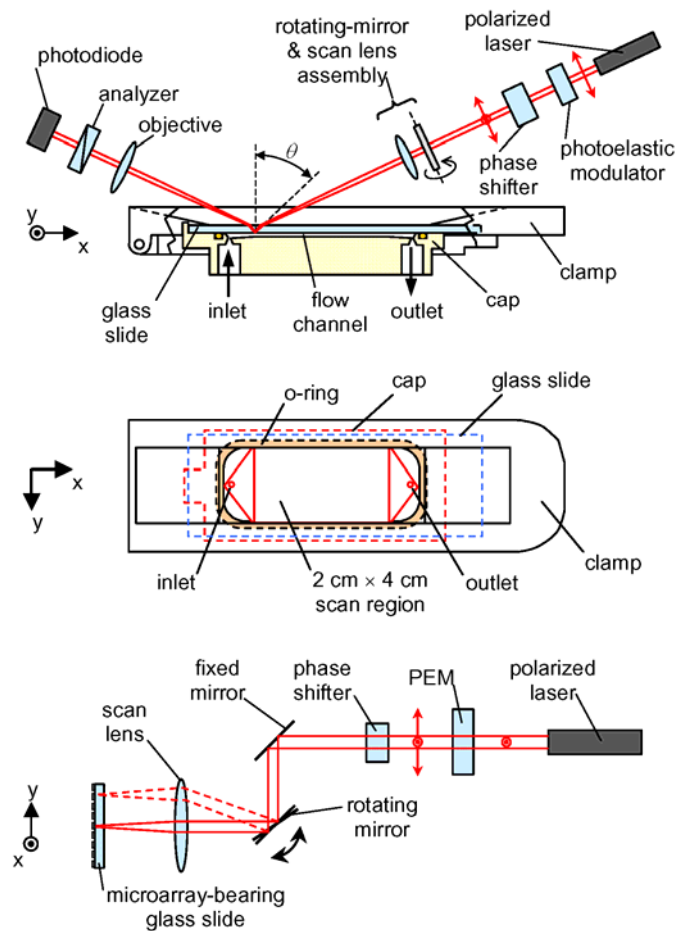
$$S(\Omega) = -I_0 J_1(\pi) H(\Omega) |r_p| |r_s| \sin(2P) \sin(2A) \sin(\delta + \Phi_{PS} + \Phi_{sys}) \quad (\text{S-1})$$

for the first harmonic and

$$S(2\Omega) = I_0 J_2(\pi) H(2\Omega) |r_p| |r_s| \sin(2P) \sin(2A) \cos(\delta + \Phi_{PS} + \Phi_{sys}) \quad (\text{S-2})$$

for the second harmonic. The other symbols in these expressions are as follows:  $I_0$  is the output intensity of the laser;  $J_1$  and  $J_2$  are Bessel functions of the first kind;  $H$  is the frequency-dependent proportionality between the laser intensity amplitude at the photodiode and the measured photocurrent amplitude;  $|r_p|$  and  $|r_s|$  are the products of the  $p$ - and  $s$ -polarization reflection/transmission coefficient magnitudes for all the surfaces in the system (including the microarray surface);  $\delta$  is the phase difference between the  $p$ - and  $s$ -polarized components due to reflection from the microarray surface;  $\Phi_{PS}$  is the phase difference due to the phase shifter; and  $\Phi_{sys}$  is the phase difference due to all the other components. Let  $\eta = S_{\max}(\Omega)/S_{\max}(2\Omega)$  where  $S_{\max}(\Omega) = -I_0 J_1(\pi) H(\Omega) \sin(2P) \sin(2A)$  and  $S_{\max}(2\Omega) = I_0 J_2(\pi) H(2\Omega) \sin(2P) \sin(2A)$ . The parameter  $\eta$  is independent of the properties of the microarray surface and can be determined by measuring the amplitudes of  $S(\Omega)$  and  $S(2\Omega)$  plotted as a function of  $\Phi_{PS}$ . This only needs to be done once because those factors that do not divide out in the ratio remain constant throughout use of the microscope. With these definitions  $S(\Omega) = \eta S_{\max}(2\Omega) |r_p| |r_s| \sin(\delta + \Phi_{PS} + \Phi_{sys})$  and  $S(2\Omega) = S_{\max}(2\Omega) |r_p| |r_s| \cos(\delta + \Phi_{PS} + \Phi_{sys})$ . Next, let  $\delta_0$  be the phase difference for a bare (unprinted) region of the microarray surface. We initially adjust  $\Phi_{PS}$  so that  $\delta_0 + \Phi_{PS} + \Phi_{sys} = 0$  (or, more generally, a multiple of  $\pi$ ), giving  $S(\Omega) = 0$  and  $S(2\Omega) = S_{\max}(2\Omega) |r_p| |r_s|$ . When a thin layer of molecules is subsequently added to the bare surface or when the focused beam is moved to a microarray spot, the photocurrent amplitudes become  $S(\Omega) \approx \eta S_{\max}(2\Omega) |r_p| |r_s| (\delta - \delta_0)$  and  $S(2\Omega) \approx S_{\max}(2\Omega) |r_p| |r_s|$ . Therefore, under this “nulling” condition of the first harmonic, the phase difference  $\Delta\delta = \delta - \delta_0$  is obtained from the measured amplitudes by  $\Delta\delta = S(\Omega)/[\eta S(2\Omega)]$ . Before each image or real-time scan, the first harmonic is “nulled” as described above at a reference location on the unprinted microarray substrate.

FIGURE S-9



**Top panel:** Optical layout of the scanning OI-RD microscope. A glass slide with a microarray printed on the bottom surface is installed in a flow channel assembly. A polarization-modulated laser beam is scanned across the microarray in the  $y$ -direction for  $y$ -scan with a combination of a rotating mirror and a scan lens, while the flow channel assembly is translated in the  $x$ -direction relative to the illumination optics for  $x$ -scan. **Middle panel:** bottom view of the flow chamber assembly showing the 2 cm  $\times$  4 cm optically accessible area on the glass slide. **Bottom panel:** side view of the scanning microscope illustrating the  $y$ -scan.

### ***Optimizing Spot Locations for Real-time Readout***

For fast real-time readout, it is essential that the encoded linear translation stage ( $x$ -direction in **Figure 2** and **Figure S-9**) does not stop much more often than the number of columns in a microarray. As a result, it is crucial that the centers of printed spots along a microarray column (fast scan direction,  $y$  direction) do not deviate from a straight line by more than the spot radii so that the fast rotating mirror raster scan can be performed at one  $x$ -coordinate per microarray column, instead of many  $x$ -coordinates for a single column of targets. Three factors affect this: (1) the diameter and morphology of printed spots, (2) the precision of the printing robot, and (3) the regularity of pin diameters and pin-to-pin separation in the print head. Item (1) is the most variable because it depends on the physicochemical properties of the glass slide surface, the printing buffer, and the dissolved target. For example, in the first experiment described in the main text the printed BSA spots had diameters ranging from 120  $\mu\text{m}$  to 140  $\mu\text{m}$ . In the second experiment, the range was even larger when printing concentrations were varied. By printing a large microarray with a single pin (data not shown), we found that the standard deviation of the spot spacing was 9  $\mu\text{m}$  due to robotic motion precision, close to the nominal 2.5  $\mu\text{m}$  digital encoder resolution of the OmniGrid 100 translation motors. For high-throughput printing of many replicate microarrays (up to 100), multiple pins must be employed. Since a readout line needs to pass through all the spots in a column printed with different pins so that the encoded linear stage only needs to stop once for the row, the centers of the pins in the print head cannot deviate from a straight line by more than the spot radius. Typical stainless steel pins used in most robotic microarray printers do not have such a precise pin-to-pin alignment. We found that silicon pins and the associated print head from Parallel Synthesis Inc (San Jose, CA) had the pin-to-pin alignment precision for our application. Our printing test showed that the standard deviation of spot centers printed with 8 silicon pins was 11  $\mu\text{m}$ , so that 99 % of the printed spot centers will fall within 55  $\mu\text{m}$ , less than one half of the spot diameter. This regularity in spot center position allows convenient specification of the readout grid and in turn enables high-speed real-time readout.

### ***OI-RD Image Processing***

The goal of microarray image analysis is to report the amount of probe-target complex formed at each spot of the microarray. For fluorescence images, this goal is achieved with the following strategies: (1) determine a grid for addressing each spot, (2) segment spot pixels from background pixels, (3) determine if a given spot location contains a valid endpoint signal, and (4) calculate the signal from the spot pixels and the local background. These strategies remain the same in principle for OI-RD images of large microarrays, yet differ significantly in implementation. First, fluorescence signals are represented by non-negative values (typically unsigned 16-bit integers and expressed in instrument-dependent arbitrary units). The OI-RD signals may take positive and negative values and although the raw OI-RD signals are acquired by digitizing an analog signal (at 16-bit resolution), the signals have an instrument-independent physical interpretation according to Eq. (1) (see the main text). Thus, it is most useful to process the OI-RD signals as floating-point values.

A second important difference is the nature of the background signals in these two types of microarray images. Fluorescence, by its nature, allows sensitive discrimination of appropriately labeled molecules. Background from autofluorescence, nonspecific binding, and artifacts such as smearing of target molecules during washing steps (“comet tails”) inevitably occur, but can be minimized in principle by optimizing the microarray fabrication and reaction protocols. After gridding and segmenting spot pixels, the typical approach to quantifying fluorescence endpoints is to subtract an average of the local background pixels from an average of the spot pixels. In contrast, *all* label-free optical detection methods, including OI-RD and surface plasmon resonance imaging, are subject to all processes that can change the phase and magnitude of a reflected optical beam. Thus, for OI-RD images, it is important to correct (subtract out) the background both globally and locally before assessing the signal of a target spot.

The third important difference is that gridding and normalization of the spot signals are often the most difficult step in fluorescence image analysis. This is because the image quantifying the *target* microarray is usually unavailable; the structure of the grid and the target density of each spot

must be deduced from one or more probe reactions. For OI-RD images, it is routine to obtain high-contrast images of a target microarray (either before or after washing away excess printed material) before reaction with a probe. As a result, the target spots are relatively easily located and gridded, greatly aiding the process of background correction necessary for OI-RD images (the most difficult step in OI-RD image analysis). We next describe the semi-automated procedures used to process OI-RD images acquired for this study.

### ***Grid Determination***

The printed, yet unprocessed microarray is installed in the microscope and scanned. The reflectance signal  $\delta R_p/R_p + \delta R_s/R_s$ , with  $R_p = |r_p|^2$  and  $R_s = |r_s|^2$  (available as the second harmonic of the polarization-modulated laser intensity in reflection), from the spots are large with almost negligible background. A line is drawn between the centroids of the bottom-left and bottom-right spots in the microarray (see **Figure 3**, main text) to determine the angle of the microarray relative to the scan axes. Angular deviations larger than one milliradian are corrected by rotating the fluidic chamber assembly with a flexure-tilt mechanism.

*First iteration readout grid.* Once the microarray axes are aligned with the scan axes, the reflectance signals  $\delta R_p/R_p + \delta R_s/R_s$  are added up along the  $y$ -axis (image pixel columns) to obtain a comb-like profile of  $x$ -coordinates, and the same signals are added up along the  $x$ -axis (image pixel rows) to obtain a comb-like profile of  $y$ -coordinates. The peak positions in these two profiles mark the average coordinates of printed spots on a rectangular grid, albeit irregularly spaced. These positions are found by fitting a quadratic equation to the profile points located in a sliding window. The fit coefficients are tested to see if the quadratic is consistent with a local maximum of sufficient height and width, and if so the peak location is calculated. These peak positions in  $x$  and  $y$  coordinates form the first iteration of the real-time readout grid. After the target channel pixels (grid points) are located, the reference channel pixels are determined by computing the midpoint between consecutive targets in the  $y$  (fast scan) direction; references at the edges of the arrays are positioned approximately half a spot spacing away.

*Second iteration readout grid.* If there is a great deal of variability in the spot diameters and the locations of the spot centroids, the average coordinates as specified in the first-iteration readout grid can miss a significant number of target spots. In this case, we make the following adjustments: The reflectance image is globally binarized (with thresholds set to the global image mean  $\pm$  one standard deviation) to segment out the spots. The image is then partitioned into rectangles centered on the original grid points, each containing a binarized target spot. We shift the readout coordinates for the spot from the geometrical center of the rectangle to the centroid of the binarized spot (if a spot is not present, the center of the box is used). These shifted coordinates form the second iteration readout grid. Our scanning software can read out this “center-of-mass relaxed” grid in real-time, and the algorithm works extremely well for small microarrays. But for large microarrays with 10,000 spots such a “center-of-mass relaxed” readout grid with a nearly random distribution of pixel positions is inefficient due to the large number of distinct  $x$  coordinates (up to 10,000 from less than 200) where the encoded linear stage needs to stop.

*Third iteration readout grid.* Thus for large microarrays, we choose the median of the “center-of-mass relaxed”  $x$  coordinates for each column of the printed targets (parallel to  $y$  axis) as the  $x$ -coordinate for the entire row, thus reducing the number of distinct target  $x$  coordinates from potentially 10,000 back to the number of target rows. Since scanning along the  $y$  direction is accomplished with a fast scan mirror, the unique  $y$  values can be kept without significant increase in total readout time. For operational reasons though, we sometimes choose the median of the “center-of-mass relaxed”  $y$  coordinates as the  $y$ -coordinates for a column of printed targets.

### ***Background Correction***

In order of decreasing length scale, the background signals in an OI-RD image (the  $\Delta\delta$  phase signal from the measurement of the first harmonic of the reflected laser beam in polarization modulation frequency) are: (1) a monotonic and nearly linear component arising from the change in incidence angle with respect to the scan mirror surface; (2) mechanical strain in the glass substrate (recall the substrate is used as a window to the flow cell); (3) inhomogeneity on the glass surface and

chemically functionalized surface coating; and (4) stochastic pixel-to-pixel noise. Nominally, backgrounds (1)-(3) are static in time and are unaffected by a reaction of the microarray. Thus, the simple means of background correction is to *subtract* an image taken before a reaction from an image taken after the reaction, revealing the change due only to the reaction (plus noise). However, in practice these backgrounds (particularly item (2)) slowly drift in time, leaving a residual background in the difference image that must be corrected. Furthermore, if one desires to extract quantitative information from a target image, these backgrounds must be corrected. Generally, our background correction results are more accurate and robust for difference images due to smaller background signals.

We start with reducing background (1) by modeling it with a 3<sup>rd</sup>-order two-dimensional polynomial and subtracting it pixel-by-pixel from the image. Let us denote the original  $\Delta\delta$  image as Image-0. Because the image is large, we do not wish to perform a computationally expensive least-squares calculation on all of the pixels. Thus, we first create a coarse-grained version of Image-0, which we will denote as Image-1. To obtain Image-1, we interpolate each row of pixels in Image-0 with cubic splines, select a sparse set of regularly spaced points along the rows (e.g. one tenth of the original pixel density along both directions), and evaluate the interpolating functions at these new locations; the process is then repeated for the other direction (pixel columns). On Image-1, we then apply simple thresholds (global image median  $\pm$  three median absolute deviations) to crudely segment out the strongest microarray spots and artifacts (air bubbles, scratches, dirt) remaining in the coarse grained image. We least squares fit the coarse grained image globally to a 3<sup>rd</sup>-order two-dimensional polynomial, excluding the segmented pixels from the previous step. The resulting polynomial is then subtracted from the original image (Image-0), pixel-by-pixel, to arrive at the globally treated image (Image-2). This essentially removes the slow varying background (1) and centers the residual background (2) about zero. By using a cubic-spline interpolation instead of a simple averaging method for the coarse graining, we can utilize the entire image including the margins and thus improve the quality of this step.

The line profiles along the rows and columns of Image-2 (obtained after the above polynomial global treatment) indicate that the remaining background is well modeled locally by, for example, 5<sup>th</sup>-order polynomials. Thus, we next partition the image into smaller blocks (typically 2 to 5 mm on a side) and within each partition least-square fit a one-dimensional 5<sup>th</sup> order polynomial to each column and/or row in the block. However, pixels from the microarray spots and other artifacts erroneously affect the fit; as a result, they need to be excluded from the fit. We have employed three methods to this end: (A) for high signal-to-noise spots, a crude global threshold may suffice. In this case, we compute the median (M-2) and the median absolute deviation (MAD-2), and use  $M-2 \pm 3 \times MAD-2$  to obtain a binary mask for exclusion of the microarray spots and other artifacts. Unfortunately, this does not always work well; (B) alternatively, we use a binary mask from global thresholding the differential reflectance image ( $\delta R_p/R_p + \delta R_s/R_s$ ) of the dry microarray (before washing) to exclude these pixels. This data is readily available, but it less convenient than other methods because it requires an extra registered image; (C) in practice, it is convenient to use Image-2 and the following strategy. The signals from microarray spots of Image-2 typically have the same sign (i.e. all spots are positive relative to local background) and the spot diameters are no more than half of the center-to-center spot spacing. A grayscale morphological top hat transformation<sup>5</sup> can be applied to it as follows. For every pixel, we replace the value by the minimum of all pixels within a square that is centered at the pixel in question and with a side width a little larger than the spot diameter; afterward we replace the value of a pixel with the maximum of all pixels again within the same sized square centered at the pixel of interest. This procedure removes the microarray spots and other small features (e.g. dirt and small bubbles) from Image-2 and replaces them with values close to the nearby background. The resulting image (Image-3) contains the background of length scales down to twice the size of the square. We subtract Image-3 from Image-2 to eliminate the background. We then find the median (M-4) and the median absolute deviation (MAD-4) of the resulting image (Image-4) to obtain a binary mask (thresholds set at  $MAD-4 \pm 3 \times MAD-4$ ). The mask is used to exclude the microarray spots and artifacts and enables us to perform within each partition the least-square fit to a one-dimensional 5<sup>th</sup> order polynomial for each column and/or row in the block. By

subtracting the polynomial fit from Image-2 for each partition, we arrive at the final background-corrected image (Image-5). This method of automatically generating a mask from the image itself with the top hat transformation was applied to all images acquired for this study.

### ***Spot Detection***

After the locations of spots have been determined and the background has been subtracted, it remains to compute the “endpoint signal” for each spot and whether the signal suggests marking the spot “hit”, “no reaction”, or some other appropriate classification. This means we need to segment spot pixels from the substrate pixels as in previous steps, but do a better job of segmenting artifact pixels from spot pixels. We note that, after applying the above background subtraction procedure, most spots can be successfully segmented from the background by globally applying thresholds equal to image median  $\pm$  three median deviations. In general, spot signals range from the detection limit (i.e. the standard deviation of the noise in the unprinted region of the glass surface) up to the detector saturation level. In our microarray images, the spot diameters are no more than half the center-to-center spot spacing and we generally image a wide margin around the microarray edge to improve the background correction. Thus, spot pixels comprise at most  $\sim 20\%$  of the image pixels. In the histogram of signals from all pixels, the signals from the background pixels form a Gaussian peak with zero mean and the signals from the spot pixels are essentially outliers (with the exception of spots near the limit of detection). The use of the median and the median absolute deviation allows the center and dispersion of the background signal distribution to be accurately estimated despite the variable, large outliers (i.e. spot and artifact pixels). To reduce the number of false positives while keeping most weak spots, we apply an improved segmentation procedure based upon local thresholding as follows.

We first apply a noise-reducing filter to the image, such as a  $3 \times 3$  Gaussian convolution mask or a  $3 \times 3$  median filter. The filters reduce false positives from the stochastic noise and small punctuate artifacts (the latter are suppressed particularly well by the median filter), and the blurring of the spot edges due to filtering has little impact on spot pixel segmentation. We then use the target

readout grid to partition the microarray into rectangular boxes, each (potentially) containing a spot and its surrounding background. Since the spot pixels comprise no more than 20% of the pixels within each partition, we computed for each partition the upper and lower thresholds equal to the partition median ( $M_p$ )  $\pm$  three median absolute deviations ( $3 \times \text{MAD}_p$ ). Pixels between the thresholds are considered background pixels while pixels outside the thresholds are considered *potential* spot pixels. As an option, if many spot pixels are nearby but disconnected, morphological closing can be applied to connect them. Likewise, morphological opening can be used to eliminate isolated single pixels. We next go through each partition and keep only the largest connected “binary region” (the smaller binary regions are likely to come from noise or artifacts). We then go through the binary regions and keep only those with an average radius greater than a specified threshold (a good value can be independently measured from the original dry target image of the microarray). Finally, we eliminate those remaining binary regions that lie too close to the partition boundaries (because genuine spots should be closer to the center of the partitions). If a partition has a surviving binary region, then we flag the target or the spot in the partition as a “hit candidate”. The binary region is used as the mask to determine the spot pixel and background pixel statistics of each partition in the unfiltered but background corrected image. Thus, we now have a background corrected image, a target readout grid, a spot mask for segmenting out the spot pixels, and spot signals, which can be used to create useful rules for scoring “hits”. For instance, we often print replicate spots of a particular target in adjacent microarray addresses. We might score a particular target as a “hit” if a majority of the adjacent replicate spots were flagged as “hit candidates” and the median of the spot signals is within acceptable thresholds.

### ***Implementation of Global Curve Fitting***

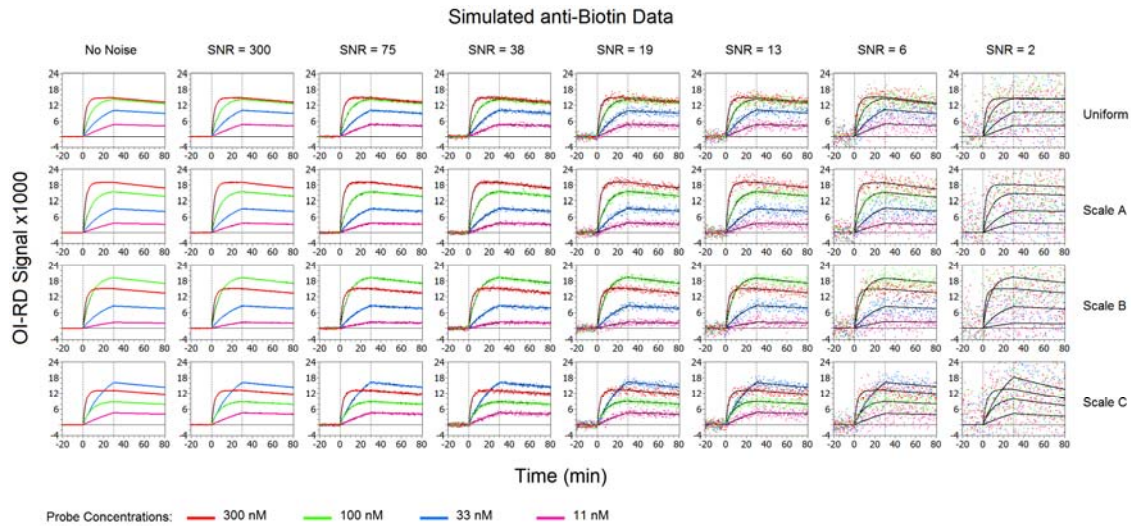
We developed a global curve fitting procedure to extract kinetic parameters of the binding reaction model from  $\sim 10,000$  binding curve sets in an efficient and automated manner. *Our goal is to match the throughput of the data analysis to the throughput of the binding curve acquisition.* After real-time data is collected, the data acquisition software compensates the raw signals, zeroes the

baselines, records the probe concentration, and records the times where association and dissociation measurements begin. Additionally, the software records instrumental noises from the baselines, endpoint signals near the completion of the association and dissociation phases, and the corresponding signal-to-noise ratios (endpoint signals divided by baseline noise). After acquiring binding curves for all probe concentrations of interest, we select the binding data files to be fit, a binding model, and a signal-to-noise threshold to determine which curve sets should be fit. The rest of the process is carried out automatically. First, binding curves from the same microarray spots (but typically different probe concentrations) are collected into sets. If the median endpoint signal-to-noise ratio of the curve set exceeds a user-set threshold, then the curve set will be fit to the binding model. We use the Levenberg-Marquardt algorithm<sup>6</sup> to find reaction model parameters that minimize the sum of square errors (SSE) between the model and *all* the curves in the set simultaneously (global curve fitting). We observe that the instrumental noise is independent of endpoint signals; as a result, we weight all data points in all curves equally in the global fit. For the one-to-one Langmuir binding model used in this study (Eq. (2a) and Eq. (2b)), common values of  $k_{on}$  and  $k_{off}$  are applied to all curves in a given set (global fit parameters), while  $\gamma N_0$  is allowed to vary for each curve (local fit parameter); the probe concentrations  $C$  and dissociation starting times  $t_0$  were recorded for each curve at the time of data acquisition. We also restrict  $k_{on}$  and  $k_{off}$  to positive values. The association and dissociation portions of the binding curves are fit simultaneously. Initial guesses for the fit parameters are obtained from a heuristic piecewise linear fit of the curves. Separate linear fits of the association and dissociation measurements converge reliably and give order of magnitude estimates of the rate constants  $k_{on}$  and  $k_{off}$ ;  $\gamma N_0$  is also estimated from these fits, or alternatively, from the association-phase endpoint signal. This initialization method allows the iterative Levenberg-Marquardt algorithm to proceed without human input and independent of the units of measurement (scaling) of the time and OI-RD values. The Levenberg-Marquardt algorithm iterates until the *change* in the sum of square errors falls below a threshold. To make the termination threshold independent of the signal scale, we set it equal to a constant ( $\sim 1 \times 10^{-6}$ ) times the maximum curve endpoint signal in the set. To increase the likelihood

that the output parameter values give a global rather than a local minimum of the sum of square errors, the heuristic initial values are randomly perturbed and input to the Levenberg-Marquardt algorithm; the output parameter set with the smallest sum of square errors is retained. The perturbations are drawn from zero-mean Gaussian distributions with standard deviations equal to the heuristic parameter value. In the present study, this was performed ten times per set of binding curves. More trials are rarely needed with the Langmuir model, *keeping the time needed to fit ~ 10,000 curve sets to ~ 1 hour* using our current computer software and hardware. Analysis time can be further reduced by fitting batches of curve sets in parallel using modern multi-core computer processors. Finally, we observe that the instrumental noise in the baseline is distributed normally, allowing us to estimate the uncertainties of the output fit parameters using the diagonal elements of the Levenberg-Marquardt output covariance matrix and the final root mean square error of the fit.

Numerical simulations of Langmuir kinetics (**Figure S-10** and **Table S-2** for a reaction with significant dissociation and **Figure S-11** and **Table S-3** for a reaction with little dissociation) with Gaussian noise and random values of  $\gamma N_0$  (to simulate the variability of microarray printing) demonstrates that our global curve fitting procedure successfully extracts meaningful values for  $k_{on}$ ,  $k_{off}$ , and  $\gamma N_0$  even for low signal-to-noise ratio ( $< 5$ ) data. After curve fitting, the output value for the off-rate,  $k_{off}$ , is further assessed as described below.

FIGURE S-10

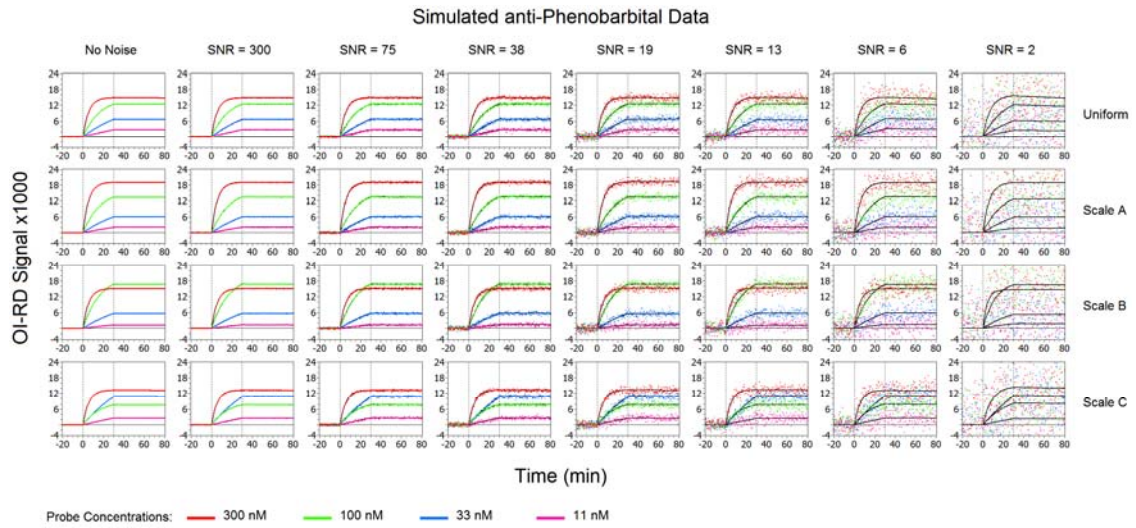


Simulated binding curves mimicking experimental data for mouse IgG reaction with biotin targets. The time interval between successive points is 25 s. The kinetic parameters are  $k_{on} = 2 \times 10^{-5} \text{ (nM}\cdot\text{s)}^{-1}$  and  $k_{off} = 4 \times 10^{-5} \text{ s}^{-1}$ . Curves were calculated for probe concentrations at 300 nM (red curves), 100 nM (green curves), 33 nM (blue curves), and 11 nM (violet curves). For the “Uniform Scale” panel, a scale factor of  $\gamma N_0 = 1.5 \times 10^{-2}$  was assumed. For the “Scale A”, “Scale B”, and “Scale C” panels, random values of  $\gamma N_0$  were drawn from a uniform distribution on the interval  $[5 \times 10^{-3}, 2.5 \times 10^{-2}]$  for each probe concentration. From highest to lowest probe concentration, the values used for “Scale A” are  $1.92 \times 10^{-2}$ ,  $1.62 \times 10^{-2}$ ,  $1.36 \times 10^{-2}$  and  $1.15 \times 10^{-2}$ ; for “Scale B”,  $1.52 \times 10^{-2}$ ,  $2.02 \times 10^{-2}$ ,  $1.26 \times 10^{-2}$ , and  $7.09 \times 10^{-3}$ ; for “Scale C”,  $1.33 \times 10^{-2}$ ,  $9.20 \times 10^{-3}$ ,  $2.41 \times 10^{-2}$ , and  $1.44 \times 10^{-2}$ . For each set of scales, curves were calculated with additive Gaussian noise with means of zero and standard deviations of  $5 \times 10^{-5}$ ,  $2 \times 10^{-4}$ ,  $4 \times 10^{-4}$ ,  $8 \times 10^{-4}$ ,  $1.2 \times 10^{-3}$ ,  $2.4 \times 10^{-3}$ , and  $2.4 \times 10^{-3}$ . The black curves show the results of globally fitting the four simulated binding curves wherein  $k_{on}$  and  $k_{off}$  are shared fit parameters, but  $\gamma$  is allowed to vary from curve to curve.

**TABLE S-2:** Global fitting parameters obtained from simulated binding curves (**Figure S-10**). For each scale and noise level, the set of four simulated binding curves was globally fit wherein  $k_{on}$  and  $k_{off}$  were shared fit parameters, but  $\gamma N_0$  was allowed to vary from curve to curve. The signal-to-noise ratio is calculated using  $SNR = 1.5 \times 10^{-2}/\text{Noise}$ , where  $1.5 \times 10^{-2}$  is the mean value of  $\gamma N_0$ . Noise is the standard deviation of the zero-mean additive Gaussian noise in the simulated data. In this case both the fitted dissociation rate constants and the association rate constants are not dominated by the noise even at  $SNR = 6$  or below.

Scale	Noise	SNR	$k_{on} \text{ (nM}\cdot\text{s)}^{-1}$	$k_{off} \text{ (s}^{-1}\text{)}$	$K_d \text{ (nM)}$
Uniform	0	$\infty$	$2 \times 10^{-5}$	$4 \times 10^{-5}$	2
	$5 \times 10^{-5}$	300	$1.996 \pm 0.004 \times 10^{-5}$	$4.00 \pm 0.01 \times 10^{-5}$	$2.004 \pm 0.008$
	$2 \times 10^{-4}$	75	$1.97 \pm 0.01 \times 10^{-5}$	$3.99 \pm 0.06 \times 10^{-5}$	$2.02 \pm 0.03$
	$4 \times 10^{-4}$	38	$1.98 \pm 0.03 \times 10^{-5}$	$4.2 \pm 0.1 \times 10^{-5}$	$2.11 \pm 0.07$
	$8 \times 10^{-4}$	19	$2.05 \pm 0.06 \times 10^{-5}$	$3.5 \pm 0.2 \times 10^{-5}$	$1.7 \pm 0.1$
	$1.2 \times 10^{-3}$	13	$1.99 \pm 0.09 \times 10^{-5}$	$3.9 \pm 0.4 \times 10^{-5}$	$2.0 \pm 0.2$
	$2.4 \times 10^{-3}$	6	$1.9 \pm 0.2 \times 10^{-5}$	$5.3 \pm 0.7 \times 10^{-5}$	$2.7 \pm 0.4$
	$7.5 \times 10^{-3}$	2	$1.9 \pm 0.5 \times 10^{-5}$	$< 4 \times 10^{-5}$	$< 2.1$
A	0	$\infty$	$2 \times 10^{-5}$	$4 \times 10^{-5}$	2
	$5 \times 10^{-5}$	300	$2.004 \pm 0.003 \times 10^{-5}$	$4.00 \pm 0.01 \times 10^{-5}$	$1.997 \pm 0.007$
	$2 \times 10^{-4}$	75	$2.00 \pm 0.01 \times 10^{-5}$	$3.97 \pm 0.05 \times 10^{-5}$	$1.99 \pm 0.03$
	$4 \times 10^{-4}$	38	$1.99 \pm 0.02 \times 10^{-5}$	$4.0 \pm 0.1 \times 10^{-5}$	$2.02 \pm 0.06$
	$8 \times 10^{-4}$	19	$1.91 \pm 0.05 \times 10^{-5}$	$4.1 \pm 0.2 \times 10^{-5}$	$2.1 \pm 0.1$
	$1.2 \times 10^{-3}$	13	$1.92 \pm 0.07 \times 10^{-5}$	$3.8 \pm 0.3 \times 10^{-5}$	$2.0 \pm 0.2$
	$2.4 \times 10^{-3}$	6	$2.2 \pm 0.2 \times 10^{-5}$	$4.4 \pm 0.6 \times 10^{-5}$	$2.0 \pm 0.3$
	$7.5 \times 10^{-3}$	2	$2.0 \pm 0.5 \times 10^{-5}$	$< 3.1 \times 10^{-5}$	$< 1.6$
B	0	$\infty$	$2 \times 10^{-5}$	$4 \times 10^{-5}$	2
	$5 \times 10^{-5}$	300	$2.006 \pm 0.003 \times 10^{-5}$	$3.98 \pm 0.01 \times 10^{-5}$	$1.982 \pm 0.007$
	$2 \times 10^{-4}$	75	$2.02 \pm 0.01 \times 10^{-5}$	$4.02 \pm 0.06 \times 10^{-5}$	$1.98 \pm 0.03$
	$4 \times 10^{-4}$	38	$1.99 \pm 0.02 \times 10^{-5}$	$3.9 \pm 0.1 \times 10^{-5}$	$1.95 \pm 0.06$
	$8 \times 10^{-4}$	19	$1.93 \pm 0.05 \times 10^{-5}$	$4.3 \pm 0.2 \times 10^{-5}$	$2.2 \pm 0.1$
	$1.2 \times 10^{-3}$	13	$2.17 \pm 0.08 \times 10^{-5}$	$3.5 \pm 0.3 \times 10^{-5}$	$1.6 \pm 0.2$
	$2.4 \times 10^{-3}$	6	$2.1 \pm 0.2 \times 10^{-5}$	$3.3 \pm 0.6 \times 10^{-5}$	$1.6 \pm 0.3$
	$7.5 \times 10^{-3}$	2	$2.3 \pm 0.5 \times 10^{-5}$	$4 \pm 2 \times 10^{-5}$	$1.6 \pm 0.9$
C	0	$\infty$	$2 \times 10^{-5}$	$4 \times 10^{-5}$	2
	$5 \times 10^{-5}$	300	$1.999 \pm 0.004 \times 10^{-5}$	$4.02 \pm 0.02 \times 10^{-5}$	$2.011 \pm 0.009$
	$2 \times 10^{-4}$	75	$2.03 \pm 0.02 \times 10^{-5}$	$4.03 \pm 0.06 \times 10^{-5}$	$1.98 \pm 0.04$
	$4 \times 10^{-4}$	38	$2.06 \pm 0.04 \times 10^{-5}$	$3.7 \pm 0.1 \times 10^{-5}$	$1.79 \pm 0.07$
	$8 \times 10^{-4}$	19	$1.93 \pm 0.07 \times 10^{-5}$	$4.6 \pm 0.2 \times 10^{-5}$	$2.4 \pm 0.2$
	$1.2 \times 10^{-3}$	13	$2.0 \pm 0.1 \times 10^{-5}$	$4.1 \pm 0.4 \times 10^{-5}$	$2.0 \pm 0.2$
	$2.4 \times 10^{-3}$	6	$1.9 \pm 0.2 \times 10^{-5}$	$3.7 \pm 0.7 \times 10^{-5}$	$1.9 \pm 0.4$
	$7.5 \times 10^{-3}$	2	$1.5 \pm 0.5 \times 10^{-5}$	$1.0 \pm 0.2 \times 10^{-5}$	$7 \pm 3$

FIGURE S-11



Simulated binding curves mimicking the anti-phenobarbital data. The kinetic parameters used are  $k_{\text{on}} = 1 \times 10^{-5} \text{ (nM}\cdot\text{s)}^{-1}$  and  $k_{\text{off}} = 8 \times 10^{-7} \text{ s}^{-1}$ . All other simulation parameters are the same as for **Figure S-10**.

**TABLE S-3:** Global fitting parameters obtained from the simulated anti-phenobarbital binding curves in **Figure S-11**. For each scale and noise level, the four simulated binding curves were globally fit wherein  $k_{on}$  and  $k_{off}$ , were shared fit parameters, but  $\gamma N_0$  was allowed to vary from curve to curve. The signal-to-noise ratio is calculated using  $SNR = 1.5 \times 10^{-2}/\text{Noise}$ , where  $1.5 \times 10^{-2}$  is the mean value of  $\gamma N_0$ . Noise is the standard deviation of the zero-mean additive Gaussian noise in the simulated data. It is clear that in this case study, the fitted dissociation rate constants are dominated by the noise even with  $SNR < 300$ , while the fitted association rate constants are not.

Scale	Noise	SNR	$k_{on}$ (nM·s) <sup>-1</sup>	$k_{off}$ (s <sup>-1</sup> )	$K_d$ (nM)
Uniform	0	$\infty$	$1 \times 10^{-5}$	$8 \times 10^{-7}$	0.08
	$5 \times 10^{-5}$	300	$1.003 \pm 0.002 \times 10^{-5}$	$5 \pm 2 \times 10^{-7}$	$0.05 \pm 0.02$
	$2 \times 10^{-4}$	75	$9.92 \pm 0.08 \times 10^{-6}$	$< 1.0 \times 10^{-6}$	$< 0.11$
	$4 \times 10^{-4}$	38	$9.8 \pm 0.2 \times 10^{-6}$	$3 \pm 1 \times 10^{-6}$	$0.3 \pm 0.1$
	$8 \times 10^{-4}$	19	$1.06 \pm 0.03 \times 10^{-5}$	$< 4.4 \times 10^{-6}$	$< 0.42$
	$1.2 \times 10^{-3}$	13	$9.2 \pm 0.4 \times 10^{-6}$	$< 6.0 \times 10^{-6}$	$< 0.65$
	$2.4 \times 10^{-3}$	6	$1.0 \pm 0.1 \times 10^{-5}$	$< 1.4 \times 10^{-5}$	$< 1.4$
	$7.5 \times 10^{-3}$	2	$8 \pm 2 \times 10^{-6}$	$< 3.9 \times 10^{-5}$	$< 5$
A	0	$\infty$	$1 \times 10^{-5}$	$8 \times 10^{-7}$	0.08
	$5 \times 10^{-5}$	300	$9.99 \pm 0.02 \times 10^{-6}$	$9 \pm 1 \times 10^{-7}$	$0.09 \pm 0.01$
	$2 \times 10^{-4}$	75	$1.000 \pm 0.007 \times 10^{-5}$	$1.5 \pm 0.6 \times 10^{-6}$	$0.15 \pm 0.06$
	$4 \times 10^{-4}$	38	$1.00 \pm 0.01 \times 10^{-5}$	$< 1.7 \times 10^{-6}$	$< 0.17$
	$8 \times 10^{-4}$	19	$9.8 \pm 0.3 \times 10^{-6}$	$< 3.4 \times 10^{-6}$	$< 0.35$
	$1.2 \times 10^{-3}$	13	$1.02 \pm 0.04 \times 10^{-5}$	$< 4.8 \times 10^{-6}$	$< 0.47$
	$2.4 \times 10^{-3}$	6	$8.9 \pm 0.7 \times 10^{-6}$	$< 1.0 \times 10^{-5}$	$< 1.2$
	$7.5 \times 10^{-3}$	2	$9 \pm 2 \times 10^{-6}$	$< 3.4 \times 10^{-5}$	$< 3.8$
B	0	$\infty$	$1 \times 10^{-5}$	$8 \times 10^{-7}$	0.08
	$5 \times 10^{-5}$	300	$9.96 \pm 0.02 \times 10^{-6}$	$1.0 \pm 0.1 \times 10^{-6}$	$0.10 \pm 0.01$
	$2 \times 10^{-4}$	75	$9.91 \pm 0.07 \times 10^{-6}$	$1.9 \pm 0.6 \times 10^{-6}$	$0.19 \pm 0.06$
	$4 \times 10^{-4}$	38	$1.00 \pm 0.02 \times 10^{-5}$	$< 2.0 \times 10^{-6}$	$< 0.20$
	$8 \times 10^{-4}$	19	$1.02 \pm 0.03 \times 10^{-5}$	$< 4.0 \times 10^{-6}$	$< 0.40$
	$1.2 \times 10^{-3}$	13	$1.04 \pm 0.05 \times 10^{-5}$	$< 6.0 \times 10^{-6}$	$< 0.58$
	$2.4 \times 10^{-3}$	6	$1.04 \pm 0.09 \times 10^{-5}$	$< 1.1 \times 10^{-5}$	$< 1.1$
	$7.5 \times 10^{-3}$	2	$1.4 \pm 0.4 \times 10^{-6}$	$< 3.8 \times 10^{-5}$	$< 2.8$
C	0	$\infty$	$1 \times 10^{-5}$	$8 \times 10^{-7}$	0.08
	$5 \times 10^{-5}$	300	$9.98 \pm 0.02 \times 10^{-6}$	$9 \pm 2 \times 10^{-7}$	$0.10 \pm 0.02$
	$2 \times 10^{-4}$	75	$9.98 \pm 0.09 \times 10^{-6}$	$< 1.2 \times 10^{-6}$	$< 0.12$
	$4 \times 10^{-4}$	38	$9.7 \pm 0.2 \times 10^{-6}$	$< 2.5 \times 10^{-6}$	$< 0.26$
	$8 \times 10^{-4}$	19	$9.7 \pm 0.4 \times 10^{-6}$	$< 4.9 \times 10^{-6}$	$< 0.51$
	$1.2 \times 10^{-3}$	13	$1.09 \pm 0.06 \times 10^{-5}$	$< 7.2 \times 10^{-6}$	$< 0.66$
	$2.4 \times 10^{-3}$	6	$1.0 \pm 0.1 \times 10^{-5}$	$< 1.5 \times 10^{-5}$	$< 1.5$
	$7.5 \times 10^{-3}$	2	$6 \pm 2 \times 10^{-6}$	$< 4.0 \times 10^{-5}$	$< 6.3$

## Estimation of an Upper Bound for the Dissociation Rates of High-Affinity Binders

A most important use of kinetic rate constants obtained from real-time binding curves is the determination of the equilibrium association constant  $K_a$ , given by  $K_a = k_{on}/k_{off}$ .  $K_a$  is the measure of the binding affinity between a probe and a target. Often the difference in  $K_a$  comes mainly from the difference in  $k_{off}$  rather than  $k_{on}$ . That is, high-affinity binding reactions have low values of  $k_{off}$  and vice versa.

For reactions with equilibrium association constants  $K_a$  larger than  $10 \text{ nM}^{-1}$ , (i.e.,  $K_d$  less than  $0.1 \text{ nM}$ ), we only report the 68% confidence *upper bounds* (the Langmuir kinetic parameters must be nonnegative). The reason is as follows: When the change in optical signal due to probe dissociation over the observation time of dissociation phase (60 minutes in this experiment) is less than the background noise in the signal, the dissociation portion of the binding curve is essentially flat and as a result  $k_{off}$  deduced from the curve-fitting is less than its standard deviation (determined by the noise from the curve-fitting). In this case, it is only sensible to use the standard deviation of  $k_{off}$  to set an upper bound for  $k_{off}$ . We next derive a simple algorithm for finding such an upper bound for the dissociation rate (and in turn the lower bound for the equilibrium association constants  $K_a$ ). It is a function of the signal-to-noise ratio, the time duration of dissociation phase, and the data-sampling rate. This notion of establishing an upper bound for  $k_{off}$  and in turn, an upper bound for  $K_a$  from experimental data applies to analysis of real-time binding curves obtained by other label-free techniques.

For binding curve measurements, an observation time up to an hour is typical. In comparison, the time for 10% of the bound probes to dissociate from the targets is  $0.1/k_{off}$ . For high-affinity reactions,  $0.1/k_{off}$  can be hours or even days. This poses a significant challenge for high-throughput binding curve measurement as the dissociation reaction observation time will need to be much less than  $0.1/k_{off}$ . In these cases, the dissociation portion of the binding curves will be more or less flat. Because the noise in the dissociation data is inevitable, the extraction of  $k_{off}$  can be dominated by the noise, namely, the uncertainty of  $k_{off}$ , rather than the fitting parameter. If the signal-to-noise ratio is too low,  $k_{off}$  from the fitting routine may vary by orders of magnitude, depending on the fitting initial

conditions and the termination threshold. Furthermore, the uncertainty in the fitted  $k_{off}$  may be larger than the fitted  $k_{off}$  itself, indicating that the latter is meaningless and the former sets a meaningful upper bound for  $k_{off}$ . We show that an *upper bound* for  $k_{off}$  is given by

$$k_{off,max} = \frac{2\sqrt{3} \cdot \sigma}{\Delta\delta(t_0) \cdot T\sqrt{N}}, \quad (\text{S-3})$$

where  $T$  is the observation time for the dissociation phase of the binding reaction,  $N$  is the number of evenly spaced measurement points of the dissociation curve,  $\Delta\delta(t_0)$  is the observed OI-RD signal at  $t = t_0$  (the beginning of the dissociation phase), and  $\sigma$  is the standard deviation of the noise in the OI-RD signal. We note that  $T$ ,  $N$ , and  $\Delta\delta(t_0)$  are readily available from the measurements. The instrumental noise  $\sigma$  can be obtained from a reference baseline acquired before the association reaction begins. This relationship is also useful for designing dissociation experiments to achieve a particular upper bound, as discussed later.

In this study, we measured  $\sim 10,000$  antibody-antigen interactions with the dissociation curves mostly flat during one-hour observation of the dissociation phase. Let the parameter values from the global curve be  $k_{on,fit}$  and  $k_{off,fit}$  and the respective uncertainties be  $\sigma_{on}$  and  $\sigma_{off}$ . In a global curve fitting, these values are common to all the curves in the fitted set. The corresponding equilibrium dissociation constant is calculated as  $K_{d,fit} = k_{off,fit}/k_{on,fit}$  with the uncertainty given by  $\sigma_d = K_{d,fit} \sqrt{(\sigma_{off}/k_{off,fit})^2 + (\sigma_{on}/k_{on,fit})^2}$ . We assume that the fit adequately describes the data such that the root mean square error (RMSE) evaluated using the fitting parameters is approximately equal to the instrumental noise,  $\sigma \approx \text{RMSE}$ , and thus  $k_{on} = k_{on,fit} \pm \sigma_{on}$  is a reasonable estimate of the association rate constant. If there is a significant decay beyond the noise during the dissociation phase, then  $k_{off} = k_{off,fit} \pm \sigma_{off}$  is a good estimate for the dissociation rate; otherwise, only an upper bound can be established. To distinguish between these two cases, we calculate values of  $k_{off,max}^{(i)}$  using Eq. (S-3) for each curve  $i = 1, \dots, M$  (where  $M$  is the number of binding curves in a set used in the global fit). In these calculations, we approximate  $\sigma$  using the RMSE calculated for the curve

under consideration. For each curve we then determine a value of  $k_{off}^{(i)}$  such that  $k_{off}^{(i)} = k_{off,max}^{(i)}$  if  $k_{off,fit} < k_{off,max}^{(i)}$ , otherwise  $k_{off}^{(i)} = k_{off,fit}$ . We assign  $k_{off,best} = \min\{k_{off}^{(i)}\}_{i=1}^M$  and  $K_{d,best} = k_{off,best}/k_{on,fit}$ . If  $k_{off,best} = k_{off,fit}$ , we report  $k_{off} = k_{off,best} \pm \sigma_{off}$  and  $K_d = K_{d,best} \pm \sigma_d$ ; otherwise we report  $k_{off} < k_{off,best}$  and  $K_d < K_{d,best}$ .

We now consider some limiting cases. If all binding curves exhibit significant decay beyond the noise level, we naturally have  $k_{off}^{(i)} = k_{off,fit}$  for all the curves. This is because  $k_{off,max}^{(i)}$  is calculated from the fit RMSE for each curve and thus  $k_{off,fit} > k_{off,max}^{(i)}$ . If all the binding curves in the dissociation phase are essentially flat, we arrive at  $k_{off,best} = \min\{k_{off,max}^{(i)}\}_{i=1}^M$ . Since the values of  $k_{off,max}^{(i)}$  are upper bounds for the true value of  $k_{off}$ , it is sensible to report the smallest of all. In this situation, the value for  $k_{off,best}$  is determined by the curve with the highest signal-to-noise ratio ( $SNR \sim \Delta\delta(t_0)/\sigma$ ) since the other parameters ( $T$  and  $N$ ) are usually the same from curve to curve. In general, some  $k_{off}^{(i)}$  are fit values and some are upper bounds. Clearly, if the minimum value of a mixed set is a fit value, then this fit value is self-consistent with upper bound values present in the set and therefore our prescription gives a sensible answer. If the minimum value of a mixed set is an upper bound, the interpretation needs caution. In this case, the data should be examined to see if there is a curve that is poorly described by the fit model due to experimental artifacts. The questionable curves should be corrected or eliminated and the fit and the subsequent analysis should be reapplied. Lastly, we note that our prescription provides robust upper bounds even in the presence of uncorrected experimental artifacts in the data. This is true because the RMSE value used in the prescription will generally be larger than the true value of the stochastic instrumental noise  $\sigma$  due to the artifacts. Numerical demonstrations of the validity of the prescription are provided with simulated Langmuir binding data with Gaussian noise in **Figure S-10**, **Figure S-11**, **Table S-2**, and **Table S-3**.

### Derivation of the Upper Bound $k_{off,max}$ for Dissociation Rate Constant

Here we derive Eq. (S-3) presented in the previous section. We also discuss the application of this equation to designing dissociation experiments. According to Eq. (2b), the OI-RD signal during the dissociation reaction ( $t > t_0$ ) is given by

$$\Delta\delta(t) = \Delta\delta(t_0)e^{-k_{off}(t-t_0)} \quad (S-4)$$

where

$$\Delta\delta(t_0) = \gamma N_0 \cdot \frac{k_{on}C}{k_{on}C + k_{off}} \left(1 - e^{-(k_{on}C + k_{off})t_0}\right). \quad (S-5)$$

We now assume that  $t - t_0 \ll 1/k_{off}$  during the entire length of the dissociation phase. The hallmark of this condition is that the observed decay is linear. Thus Eq. (S-4) can be approximated as  $\Delta\delta(t) \approx a + b(t - t_0)$ , where  $a = \Delta\delta(t_0)$  and  $b = -\Delta\delta(t_0) \cdot k_{off}$ . The dissociation rate  $k_{off} = -b/a$  can be obtained from a linear least squares fit of the dissociation data<sup>6</sup>. The linear least squares fit also yields estimates for the slope uncertainty  $\sigma\{b\}$  and intercept uncertainty  $\sigma\{a\}$ , giving the uncertainty in the dissociation rate as  $\sigma\{k_{off}\} = k_{off} \sqrt{(\sigma\{a\}/a)^2 + (\sigma\{b\}/b)^2}$ , by propagation of errors. Let  $N$  be the number of measurements (readouts) made during the dissociation reaction,  $\Delta t$  be the time between successive measurements (readouts), and  $T = (N - 1)\Delta t$  be the total duration of observation. Furthermore, let  $\sigma = \sigma\{\Delta\delta\}$  be the uncertainty in each OI-RD observation (i.e. the instrumental noise). For large values of  $N$  (i.e.  $N > \sim 20$ ), the standard equations for the uncertainties (see, for example, Eq. 6.23 in Reference 6) reduce to  $\sigma\{b\} \approx (2\sqrt{3}\sigma)/(T\sqrt{N})$  and  $\sigma\{a\} \approx (2\sigma)/\sqrt{N}$ . Therefore the uncertainty in the dissociation rate constant is

$$\sigma\{k_{off}\} \approx \frac{2\sigma}{\Delta\delta(t_0)\sqrt{N}} \sqrt{3/T^2 + k_{off}^2} \approx \frac{2\sqrt{3} \cdot \sigma}{\Delta\delta(t_0) \cdot T\sqrt{N}}. \quad (S-6)$$

If  $k_{off} = -b/a < \sigma\{k_{off}\}$ , only  $\sigma\{k_{off}\}$  is meaningful and sets an *upper bound* for the true value of  $k_{off}$  as

$$k_{off,max} = \frac{2\sqrt{3} \cdot \sigma}{\Delta\delta(t_0) \cdot T \cdot \sqrt{N}}. \quad (S-7)$$

It is notable that all the parameters in this equation are obtainable from the data. If  $k_{on}C \gg k_{off}$ ,  $\Delta\delta(t_0) \approx \gamma N_0 \cdot (1 - e^{-k_{on}Ct_0})$  in Eq. (S-7). Since  $\gamma N_0$  is the OI-RD signal at the equilibrium, a useful definition of the signal-to-noise ratio of the data is  $SNR = \gamma N_0 / \sigma$ . In this case, Eq. (S-7) can be rewritten as

$$k_{off,max} \approx \frac{2\sqrt{3} \cdot \sqrt{\Delta t}}{T^{3/2} \cdot SNR \cdot (1 - e^{-k_{on}Ct_0})}. \quad (S-8)$$

This form is useful for designing dissociation experiments. A smaller value of  $k_{off,max}$  gives a tighter bound on  $k_{off}$  and therefore Eq. S-8 makes it clear that short sampling periods, long observation times, and high signal-to-noise ratios are desirable, as intuitively expected. The smallest achievable sampling period  $\Delta t$  is limited by the scanning hardware and the number of microarray spots to be read out; thus  $\Delta t$  is not very convenient for tuning  $k_{off,max}$ . It should be pointed out that smoothing the data, such as by convolution or median filters, to increase the apparent SNR does not reduce  $k_{off,max}$ . This is because smoothing operations also increase the effective value of  $\Delta t$  by a factor of the half-width of the smoothing window, canceling out the gain in SNR (which scales roughly as the square root of the window half-width). Therefore tuning  $k_{off,max}$  through SNR must come through boosting the signal, such as by increasing the surface density of binding sites  $N_0$ . Additionally, one can boost the signal by choosing probe concentration  $C$  or association reaction duration  $t_0$  to bring the association signal near equilibrium ( $e^{-k_{on}Ct_0} \sim 0$ ). Lastly, one can choose to observe the dissociation reaction for a longer time. Since  $\Delta t$  is a constant for all practical purposes, Eq. (S-8) shows that  $k_{off,max} \propto T^{-3/2}$ . For example, a 100-fold decrease in  $k_{off,max}$  requires a 20-fold increase in observation time.

## SUPPLEMENT REFERENCES

1. Landry, J. P., Zhu, X. D. & Gregg, J. P. Label-free detection of microarrays of biomolecules by oblique-incidence reflectivity difference microscopy. *Optics Letters* **29**, 581-3 (2004).
2. Fei, Y. Y. et al. A novel high-throughput scanning microscope for label-free detection of protein and small-molecule chemical microarrays. *Review of Scientific Instruments* **79**, 013708-7 (2008).
3. Zhu, X. et al. Oblique-incidence reflectivity difference microscope for label-free high-throughput detection of biochemical reactions in a microarray format. *Applied Optics* **46**, 1890-1895 (2007).
4. Landry, J. P., Sun, Y. S., Lam, K. S. & Zhu, X. D. High-Throughput Endpoint and Real-Time Detection of Biochemical Reactions in Microarrays Using Label-Free Oblique-Incidence Reflectivity Difference Microscopes. *Conference on Lasers and Electro-Optics/Quantum Electronics and Laser Science Conference and Photonic Applications Systems Technologies*, CTuV7 (2007).
5. Gonzalez, R. C. & Woods, R. E. *Digital image processing* (Prentice Hall, 2002).
6. Bevington, P. R. & Robinson, D. K. *Data Reduction and Error Analysis for the Physical Sciences* (McGraw-Hill, 1992).